UNIVERSITY OF TURKU

Pharmacokinetics of a Novel CB_1 Receptor Imaging Tracer [^{18}F]FPATPP in Different Rat Strains

Site of research:
Preclinical Imaging, Turku PET Centre,
University of Turku, Turku, Finland

Master's Thesis

Author:
Paula Lehtinen, pakril@utu.fi

Supervisors:
Adjunct professor Francisco R. López-Picón
Adjunct professor Merja Haaparanta-Solin

09.05.2023
Turku, Finland

Master's thesis

Subject: Institute of Biomedicine, MDP in Biomedical Sciences, Drug Discovery and Development
Author: Paula Lehtinen
Title: Pharmacokinetics of a Novel CB1 Receptor Imaging Tracer [^{18}F]FPATPP in Different Rat Strains
Supervisors: Adj. prof. Francisco R. López-Picón and Adj. prof. Merja Haaparanta-Solin
Number of pages: 36 pages
Date: 09.05.2023

The endocannabinoid system is an internal regulatory system in humans that plays a role in several diseases, including neurodegenerative disorders. It consists of endocannabinoids, enzymes, and two types of cannabinoid receptors, CB1R and CB2R. This study aimed to investigate the pharmacokinetics of a new CB1R-specific positron emission tomography (PET) radiotracer called [^{18}F]FPATPP, developed at the Turku PET Centre, in male and female rats of four different strains using both *in vivo* PET and computerized tomography (CT) imaging, and *ex vivo* brain autoradiography.

The experiment used male and female rats aged two to three months from the Fischer344, Sprague Dawley, Wistar, and Lewis strains. The rats were cannulated under isoflurane/oxygen anesthesia and underwent a 10-minute CT scan before a dynamic 120-minute PET scan in an Inveon PET/CT scanner started after injecting [^{18}F]FPATPP (20 ± 5 MBq). After PET imaging, the rats were euthanized, and their brains were snap-frozen and sectioned coronally. The brain slices were then exposed to photostimulable phosphor imaging plates, and the imaging plates were digitalized using Fuji BAS5000 scanner. The *in vivo* PET images were analyzed as standardized uptake values (SUVs) as ratios to the reference brain region pons. In addition, some peripheral organs and tissues were collected and measured for radioactivity by using a 2480 Wizard2 automatic gamma counter. The autoradiographic analyses were performed manually for 13 brain regions of interest as a ratio to the pons.

The results of *in vivo* PET imaging showed that Fischer344 rats had higher initial tracer uptake in both sexes compared to the other strains. The highest peak-to-120-min ratios and SUV ratios to pons, indicating the tracer washout, were observed in Sprague Dawley males and Wistar females. The [^{18}F]FPATPP uptake in the whole brain measured at 100-120 min after injection showed significant differences mainly between Fischer344 and Sprague Dawley male rats. Autoradiography data of specific brain regions showed generally lower SUV ratios to pons in Fischer344 male compared to the other stains causing differences between both strains and sexes. The most significant differences were detected in the globus pallidus, substantia nigra's dorsal part, and cerebellum gray matter. *Ex vivo* biodistribution uptake was observed in CB1R-rich organs such as the brain and brown adipose tissue, as well as metabolic organs such as the small intestine and liver.

The study highlights the importance of strain and gender selection when evaluating the pharmacokinetics of a PET tracer, as significant differences were observed between strains and sexes in all the analyses. The most significant difference was observed between Fischer344 and Sprague Dawley rats. Radiometabolite and CBR1 blocking studies are needed to fully understand the pharmacokinetics of [^{18}F]FPATPP in rats.

Key words: Cannabinoid receptor, tracer, PET-imaging, autoradiography

Table of contents

1 Introduction

1.1 Endocannabinoid system

The endocannabinoid system is the endogenous regulation system of humans and other vertebrates. This system was found in the 1980s by Howlett and Devane (Devane et al., 1988) and ever since, it has been under investigation for multiple purposes. Endocannabinoid system contains cannabinoid receptors 1 and 2 (CB1R and CB2R, together CBRs), endogenous ligands of those receptors called as endocannabinoids, and enzymes which are responsible of biosynthesis and degradation of the endocannabinoids. (Mechoulam and Parker, 2013).

CBRs are part of the G-protein coupled receptor family, which means that they have cytoplasmic C-terminus, seven trans-membrane domains and extracellular N-terminus. CB1Rs can be found from the presynaptic neurons of the central nervous system (CNS) area. (Pertwee, 2015). Typical high-density locations of CB1Rs in the brain are the caudate putamen, globus pallidus, hippocampus, substantia nigra and cerebellum gray matter but there are also many other moderate- and low-density locations (Moldrich and Wenger, 2000). Since these receptors are located in various areas of the brain, are CB1Rs part of many processes like cognition, motoric, senses and emotions (Pertwee, 2015). CB1Rs have been also found from peripheral nervous system areas and some organs like the heart, spleen, brown adipose tissue and endocrine glands, such as adrenals (Pertwee, 2015; Pagotto et al., 2006; Surkin et al., 2018). In addition, mesenchymal stem cells, which are presented in the bone marrow, have been shown to express CBRs (Howlett et al., 2002). CB2Rs instead are found mainly from immune cells but they have been also found from some neurons. The activation of CB2Rs in immune cells leads to cytokine release and cell migration in the brain and periphery. (Pertwee, 2015).

The endocannabinoids, anandamide (AEA) and 2-arachidonoyl-glycerol (2-AG), are synthetized from the lipid constituents of the cell membrane for ‘on-demand’ in the postsynaptic terminal where AEA is also degraded. Unlike AEA, 2-AG is degraded in the presynaptic terminal, the same place where a signal cascade takes a place when CBR is activated by a ligand. In the case of endocannabinoid system and CBRs, a ligand can be one of the endocannabinoids, phytocannabinoids such as Δ9-tetrahydrocannabinol (THC), or other CBR-specific substances, such as drugs and radiotracers. (di Iorio et al., 2013). Interestingly in the case of CB1Rs, release of endocannabinoids from the postsynaptic neurons acts as a rapid, retrograde signal which leads to activation of the presynaptic CB1Rs and inhibition of

transmitter release. (Ohno-Shosaku et al., 2001). The endocannabinoid system and its metabolism are illustrated in the Figure 1.

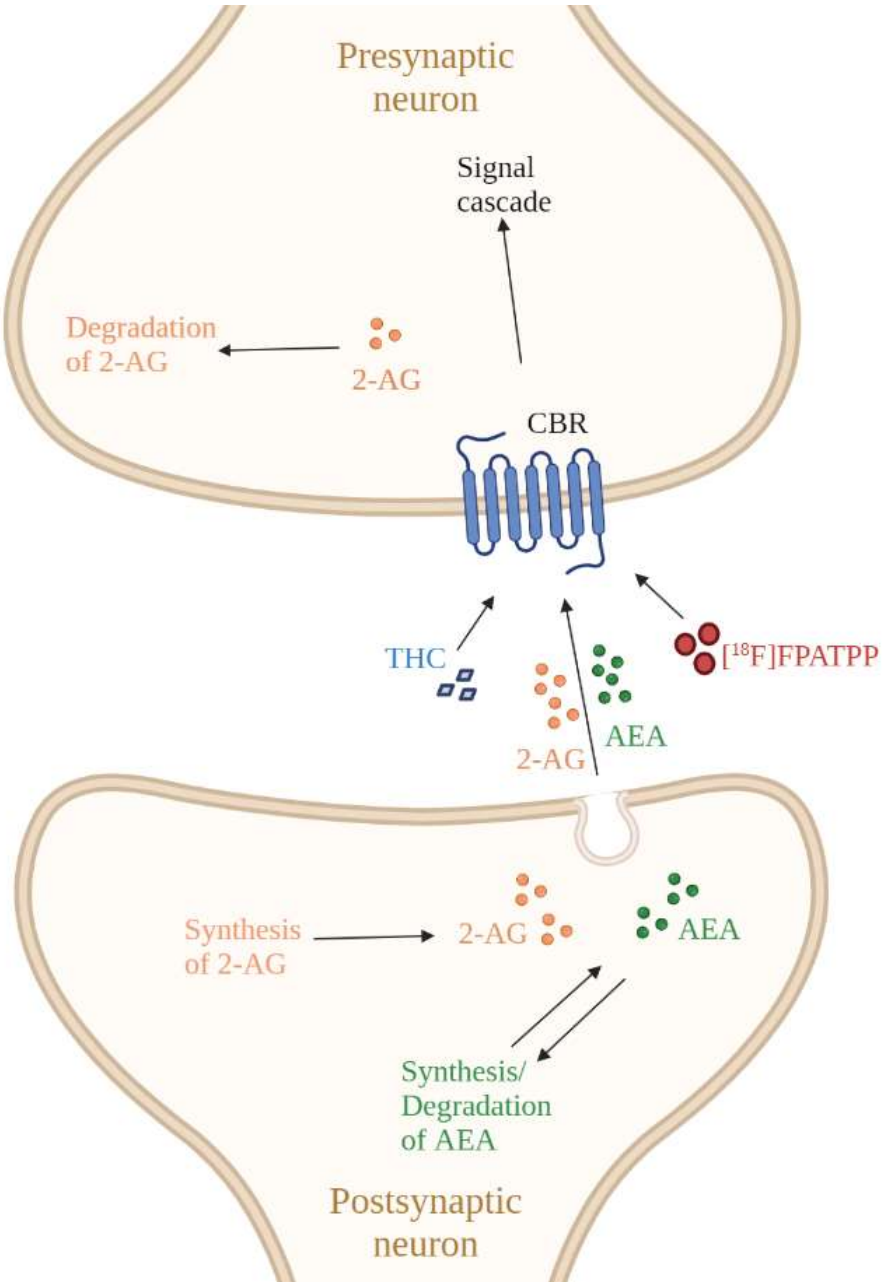

Figure 1. Endocannabinoid system. Anandamide (AEA) and 2-arachidonoyl-glycerol (2-AG) are synthetized in the postsynaptic neuron in which AEA is also degraded. AEA, 2-AG, Δ9-tetrahydrocannabinol (THC) and CB1R-specific radiotracer [^{18}F]FPATPP act trough cannabinoid receptors (CBRs) in the presynaptic neuron where 2-AG is also degraded. Created with BioRender.com.

The endocannabinoid system is involved in various physiological processes such as in motoric, metabolism, immunological events, behavior, cognition, and sensation. This system acts normally in healthy individuals, but it has been shown to be dysregulated or hypofunctional in some diseases. For example, endocannabinoid system has been shown to be hypofunctional in neurodegenerative diseases such as Alzheimer's disease and Parkinson's disease. (di Iorio et

al., 2013). On the other hand, overactive endocannabinoid system has been linked to contribution of diabetes (Gruden et al., 2016). Therefore, endocannabinoid system is a potential target for the treatment of these diseases but also other various diseases and symptoms such as mood and anxiety disorders, pain management, inflammation, cardiovascular disorders, and stroke (Lowe et al., 2021).

1.2 Positron emission tomography

Positron Emission Tomography (PET) is a widely used, non-invasive method for molecular imaging. The first PET related development steps were taken in the late 1920s, but the same kind of instrumentation as today were not used until the mid-1970s (Rich, 1997). Naturally, PET imaging techniques and scanners have been developed ever since. In principle, a radiopharmaceutical is injected intravenously *in vivo,* and it is taken up by target organs and tissues. Gamma signals emitted by the radionuclide are detected by PET scanner which converts the signals into 3D images on the computer. This basic principle of PET is illustrated in the Figure 2. In addition to actual PET imaging, whole process includes radionuclide production, radiopharmaceutical chemistry, quality control of the final product, and image analysis after imaging. (Hooker and Carson, 2019).

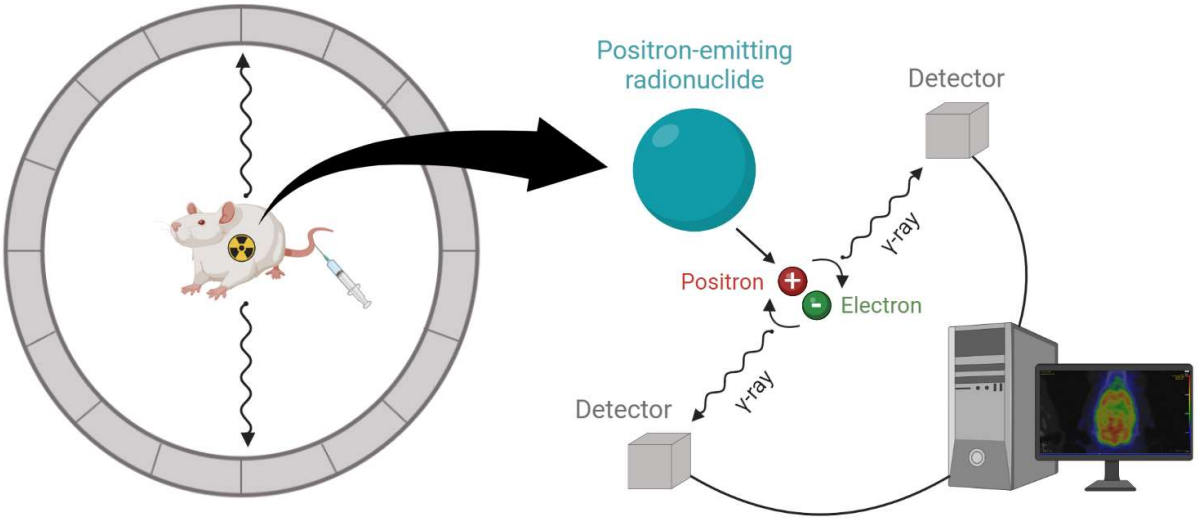

Figure 2. Illustration of the basic principle of positron emission tomography (PET) imaging. Created with BioRender.com.

PET imaging is a highly sensitive technique by which pharmacological and biochemical processes can be quantified *in vivo*. By PET, drug development for multiple conditions, such as CNS related diseases and metabolic disorders, have become easier. One of the research subjects can be the endocannabinoid system and more closely CBRs. CB1R expression, which

is compromised in many diseases, can been monitored with PET imaging. For that purpose, several ^{11}C- and ^{18}F-labeled CB1R-specific radiotracers have been developed previously, such as [^{11}C]-MePPEP, [^{18}F]MK-9470, and [^{18}F]FMPEP-d2 (Donohue et al., 2008; Yasuno et al., 2008; Burns et al., 2007). In the case of fluorine-18, its physical properties make it especially good radionuclide for PET imaging. For example, physical half-life of fluorine-18 is 109.7 min, which gives more time to perform the investigations (Hargreaves and Rabiner, 2014).

Interestingly, there are some tissues and organs which are more sensitive to radioligands and can therefore have a high accumulation detected without relation to a target. This can cause artifacts to *in vivo* PET images and needs to be considered in the data analysis phase. One of them is the Harderian glands, which humans don't have but some animals, such as rodents do. Function of the Harderian glands is not fully known, but they are found from animals, which have nictitating membranes and therefore the main indication is to excrete a lubrication for the eyes. (Brammer et al., 2007; Kiessling et al., 2017).

1.2.1 [^{18}F]FPATPP tracer

The radiotracer of this study, [^{18}F]FPATPP, is an analogue of [^{18}F]FMPEP-*d2***,** which is a well-known second-generation CB1R-specific tracer (Figure 3). [^{18}F]FMPEP-*d2* is an inverse agonist for CB1Rs and it was discovered in 2008 by Donohue et al. (Donohue et al., 2008). [^{18}F]FMPEP-*d2* has been used for example for imaging of the brown adipose tissue, studying CB1R relation to alcohol dependence and in Alzheimer's disease research (Eriksson et al., 2015; Hirvonen et al., 2013; Takkinen et al., 2018). [^{18}F]FPATPP, an inverse agonist as its analogue, was introduced by Lahdenpohja et al. (2020) when they synthesized the tracer and tested it in mice. Their aim was to test the specificity of this novel tracer by blocking the brain uptake with CB1R antagonist, rimonabant. Their study revealed that [^{18}F]FPATPP is specifically bound to CB1R in the mouse brain. Compared to [^{18}F]FMPEP-*d2,* [^{18}F]FPATPP had some improvements such as lower defluorination levels and faster washout. (Lahdenpohja et al., 2020). Both, Takkinen with [^{18}F]FMPEP-*d2* and Lahdenpohja with [^{18}F]FPATPP, used thalamus as a pseudo-reference region based on the low number of CB1Rs in that region in the mouse brain (Lahdenpohja et al., 2020; Takkinen et al., 2018).

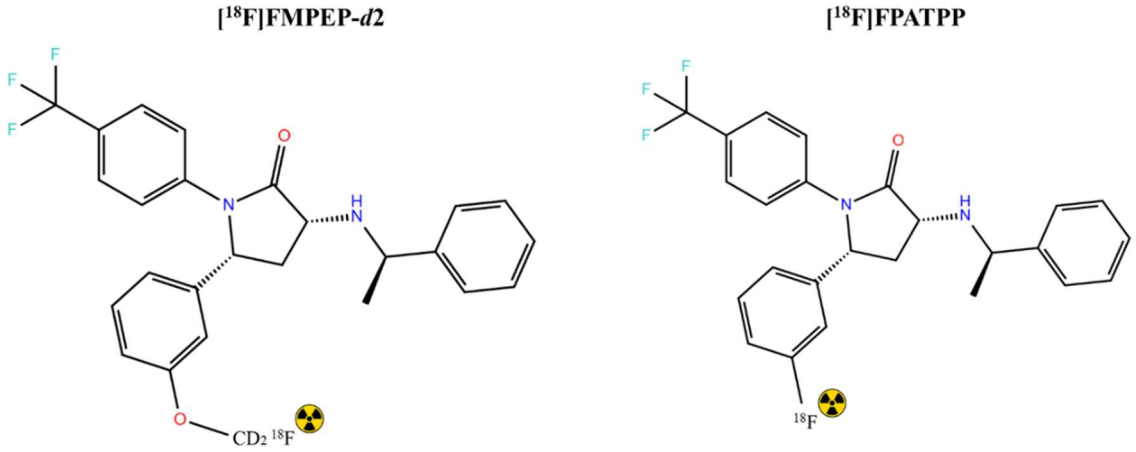

Figure 3. [^{18}F]FPATPP is an analogue of [^{18}F]FMPEP-d2. Illustrations of the molecules are created with Maestro 13.1 (Schrödinger).

[^{18}F]FPATPP is produced by a ruthenium-mediated late-stage radiofluorination method. It is based on the method of transition-metal-assisted ^{18}F-deoxyfluorination of phenols which was first published by Beyzavi et al in 2017 (Beyzavi et al., 2017). Following substances are needed for the synthesis: FPATPP precursor, ruthenium complex (CpRu(COD)Cl), and no-carrier added [^{18}F]fluoride, and these substances are added in the certain order at the certain conditions. Lahdenpohja et al. optimized this synthesis process of [^{18}F]FPATPP in their study ending up with reasonable synthesis time and good radiochemical yield with this novel imaging tracer of CB1Rs (Lahdenpohja et al., 2020).

1.3 Rat strains

Four different non-gene modified rat strains were used in this study. Sprague Dawley is an outbred, meaning that parents are not closely related, rat strain, and it is widely used in biomedical research, for example in pharmacological and toxicological studies. In addition, outbred Wistar rats were used, and they have the same kind of use than Sprague Dawley rats. Lewis is an inbred, also known as sibling mating, rat strain, and they are used for a development of animal models of multiple sclerosis and in immunological and diabetes mellitus related research. (Taconic Biosciences, 2021). Also, an inbred Fisher344 rat strain was used in this project. Interestingly, one of the few existing rat models of Alzheimer's disease was created in Fisher344 rat strain (Cohen et al., 2013). In addition, Fisher344 rats are widely used in toxicological and cancer studies as well as in aging-related studies (Taconic Biosciences, 2021).

In the previous studies, differences have been reported in the blood-brain-barrier permeability between species (Syvänen et al., 2009) and even between animal strains (Qiao et al., 2020).

More specifically, CB1R action has also been shown to differ between sexes. Takkinen et al (2018) showed this phenomenon right in their study where CB1R levels were studied in Alzheimer's disease mice (Takkinen et al., 2018). These differences make it extremely important to study both sex and strain differences but also different species as a model when starting to validate new radiotracers and to choose animal models to be used in different studies.

1.4 Aims of the research

The primary goal of this study was to characterize the pharmacokinetics of the novel radiotracer [^{18}F]FPATPP in four different rat strains, with a focus on its initial uptake, distribution, and washout in both the brain and periphery. The study also aimed to investigate potential sex and strain differences in [^{18}F]FPATPP binding between male and female rats.

2 Results

2.1 *In vivo* PET images indicated differences in the tracer uptake and washout

The results of *in vivo* PET imaging showed higher initial tracer brain uptake in both sexes of Fischer344 compared to the other rat strains, as shown in the Figure 4 and Figure 5. These figures are indicating standardized uptake values (SUVs) of the whole brain area in male and female rats, respectively. In addition, SUV time activity curves of the other strains were closer to each other than Fischer344 to any of those at the later timepoints. Interestingly, the lowest uptake at the later timepoints in male rats were seen with Sprague Dawley whereas in females the lowest uptake was with Lewis rats. The same trends were systemically seen also in the other analysed brain areas of male (Figure 6) and female (Figure 7) rats, except in the lowest uptake at the later timepoints, which was rather even between female Sprague Dawley, Wistar and Lewis rats.

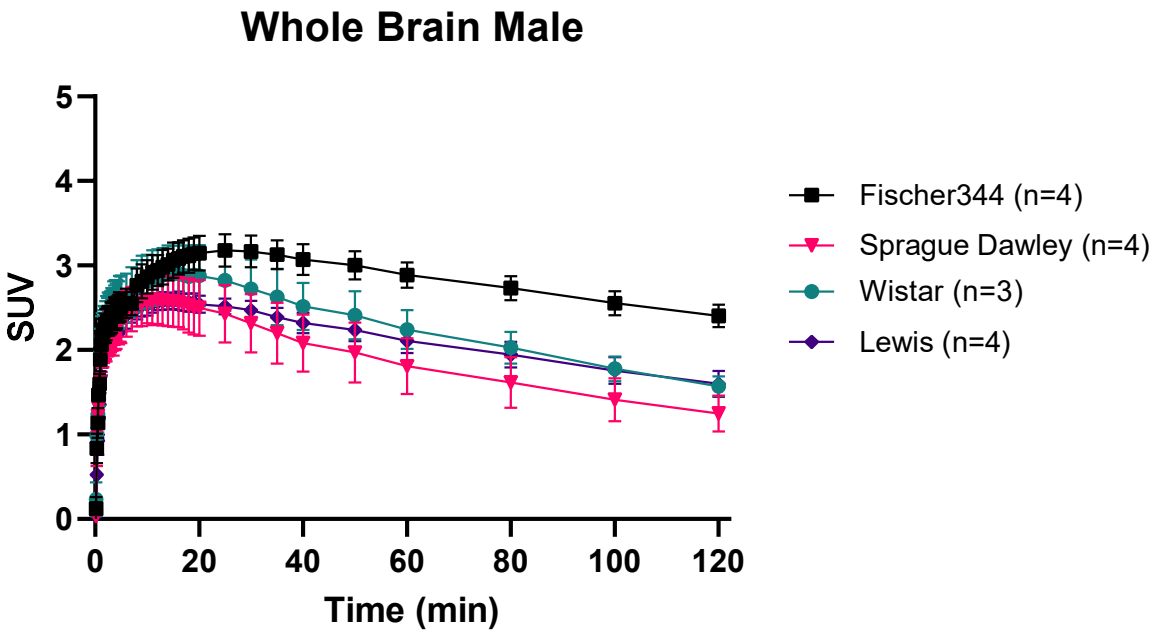

Figure 4. Standardized uptake values (SUVs) of the whole brain area in male rats.

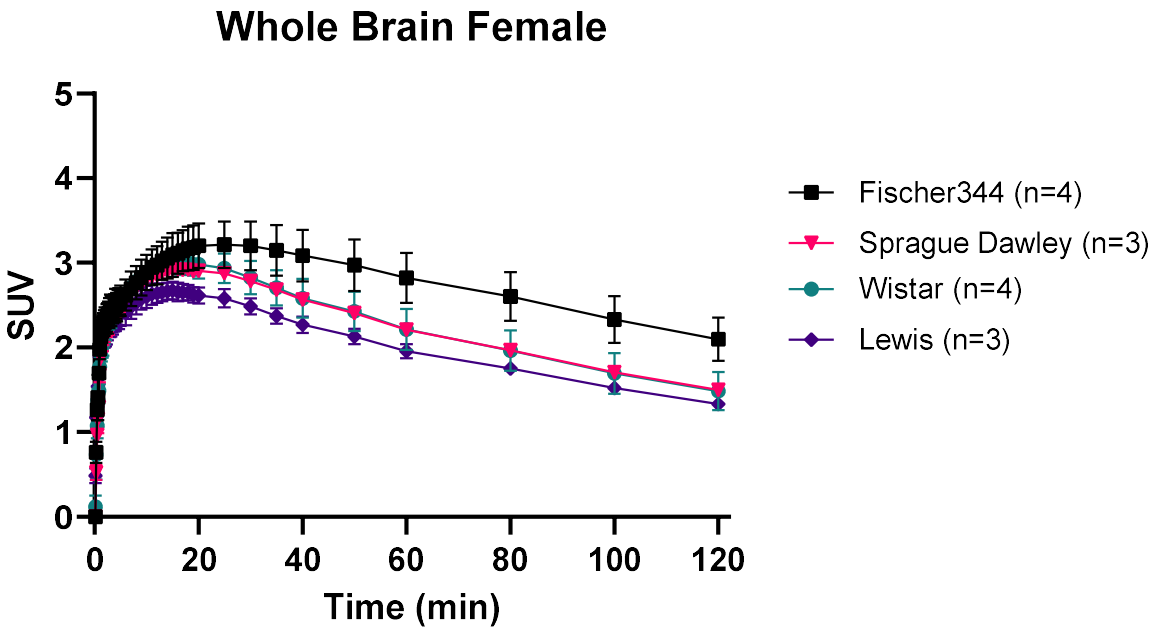

Figure 5. Standardized uptake values (SUVs) of the whole brain area in female rats.

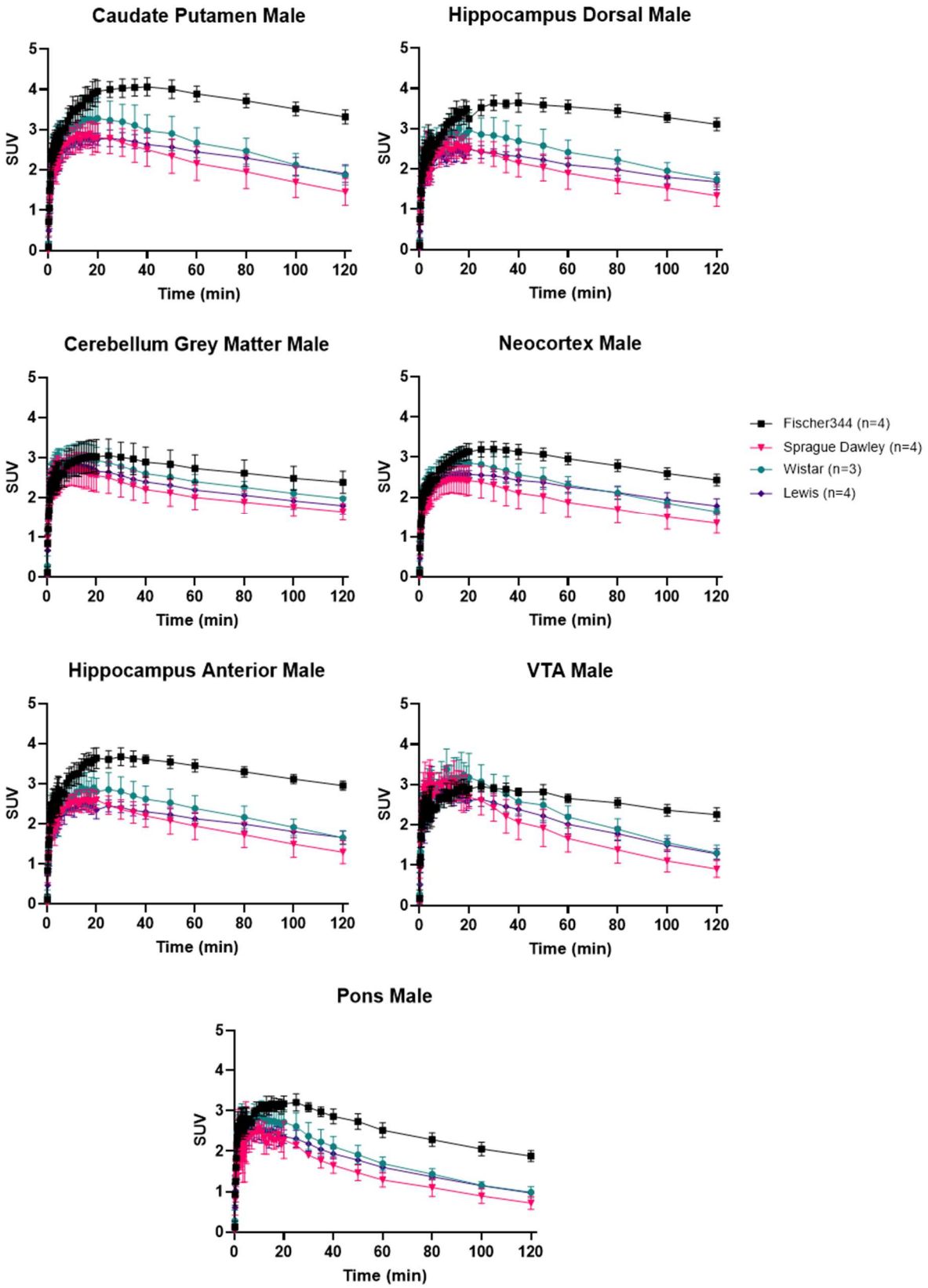

Figure 6. Standardized uptake values (SUVs) of the caudate putamen, cerebellum grey matter, hippocampus anterior and dorsal, neocortex, ventral tegmental area (VTA) and pons in male rats.

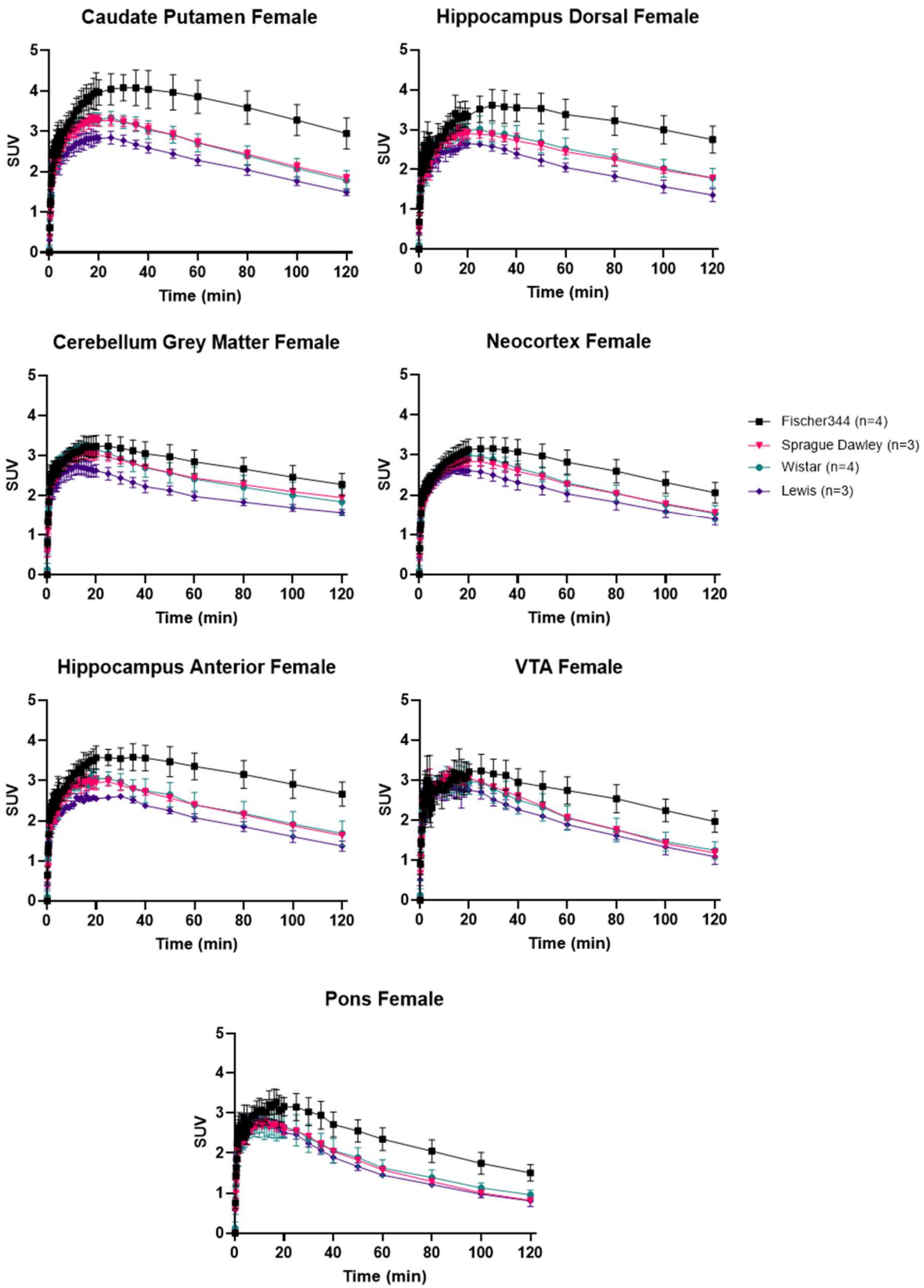

Figure 7. Standardized uptake values (SUVs) of the caudate putamen, cerebellum grey matter, hippocampus anterior and dorsal, neocortex, ventral tegmental area (VTA) and pons in female rats.

To quantify the SUV time activity curves, the area under the curve (AUC) was calculated for the whole brain area data (Table 1). Comparison calculations showed multiple significant differences (****p ≤ 0.0001) between strains and sexes (Table 2). Both sexes of Fischer344 showed difference to all the other strains. Interestingly, there were no difference between sexes inside the strains except with Sprague Dawley rats.

Table 1. Area under the curve (AUC) results of the standardize uptake value (SUV) data of the whole brain area. SE = standard error, n = number of animals.

	Fischer344 male	Fischer344 female	Sprague Dawley male	Sprague Dawley female	Wistar male	Wistar female	Lewis male	Lewis female
AUC	335.4	325.6	224.1	266.1	269.4	268.1	252.2	239.3
SE	4.16	7.81	8.06	1.27	5.65	6.44	4.10	2.09
n	4	4	4	3	3	4	4	3

Table 2. Significant differences between strains and sexes of the area under the curve (AUC) data. One-way ANOVA and Tukey´s multiple comparison test were conducted. Significant (95% confidence interval) differences between strains are marked with *p ≤ 0.05, **p ≤ 0.01, ***p ≤ 0.001, ****p ≤ 0.0001.

	Fischer344 male	Fischer344 female	Sprague Dawley male	Sprague Dawley female	Wistar male	Wistar female	Lewis male	Lewis female
Fischer344 male		ns	****	****	****	****	****	****
Fischer344 female	ns		****	****	****	****	****	****
Sprague Dawley male	****	****		****	****	****	****	*
Sprague Dawley female	****	****	****		ns	ns	ns	***
Wistar male	****	****	****	ns		ns	*	****
Wistar female	****	****	****	ns	ns		*	****
Lewis male	****	****	****	ns	*	*		ns
Lewis female	****	****	*	***	****	****	ns	

Peak to 120 min ratios were calculated to be able to quantify more specifically the later timepoints of the SUV data. These ratios are indicating the tracer washout. The highest tracer washout ratios in different brain areas were with Sprague Dawley male rats and between Wistar and Lewis female rats. The lowest tracer washout ratios were with Fischer344 rats in both sexes in all brain areas. The washout ratios of male rats are summarized in Table 3., and female rats in Table 4.

Table 3. Peak to 120 min ratios of standardized uptake values in the whole brain, caudate putamen, cerebellum grey matter, hippocampus anterior and dorsal, neocortex, ventral tegmental area (VTA) and pons of male rats.

	Fischer344 male	Sprague Dawley male	Wistar male	Lewis male
Whole brain	1.32	2.08	1.85	1.61
Caudate putamen	1.22	1.99	1.76	1.46
Cerebellum grey matter	1.28	1.65	1.53	1.57
Hippocampus anterior	1.24	2.01	1.76	1.55
Hippocampus dorsal	1.17	1.95	1.72	1.48
Neocortex	1.32	1.82	1.75	1.45
VTA	1.31	3.56	2.59	2.28
Pons	2.17	3.41	2.90	3.55

Table 4. Peak to 120 min ratios of standardized uptake values in the whole brain, caudate putamen, cerebellum grey matter, hippocampus anterior and dorsal, neocortex, ventral tegmental area (VTA) and pons of female rats.

	Fischer344 female	Sprague Dawley female	Wistar female	Lewis female
Whole brain	1.53	1.95	2.02	2.01
Caudate putamen	1.38	1.79	1.87	1.91
Cerebellum grey matter	1.42	1.57	1.75	1.75
Hippocampus anterior	1.35	1.83	1.84	1.92
Hippocampus dorsal	1.31	1.68	1.72	1.96
Neocortex	1.53	1.82	1.95	1.90
VTA	1.64	2.68	2.50	2.72
Pons	1.70	3.63	2.90	2.71

The [^{18}F]FPATPP uptake in the whole brain, measured at 100-120 min after injection, showed significant differences between Fischer344 and Sprague Dawley male rats (Figure 8.). The same difference is seen in the other analyzed brain areas (Figure 9.). Significant differences were not seen between female rats. Interestingly, sex differences were not seen inside the strain but there was a significant difference between Fischer344 male and Lewis female rats in the whole brain, caudate putamen, neocortex, anterior and dorsal parts of the hippocampus, but also between Fischer344 female and Sprague Dawley male rats in the ventral tegmental area (VTA), and anterior and dorsal parts of the hippocampus.

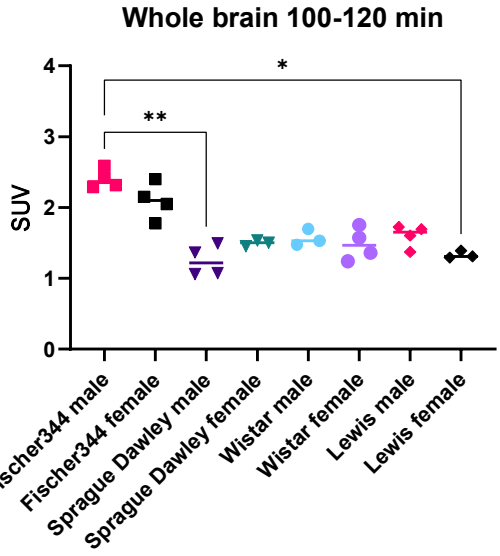

Figure 8. Standardize uptake value (SUV) of the whole brain area at 100-120 min after [^{18}F]FPATPP injection. Data are presented with median line. Kruskal-Wallis test was conducted and significant (95% confidence interval) differences between strains are marked with *p ≤ 0.05, **p ≤ 0.01.

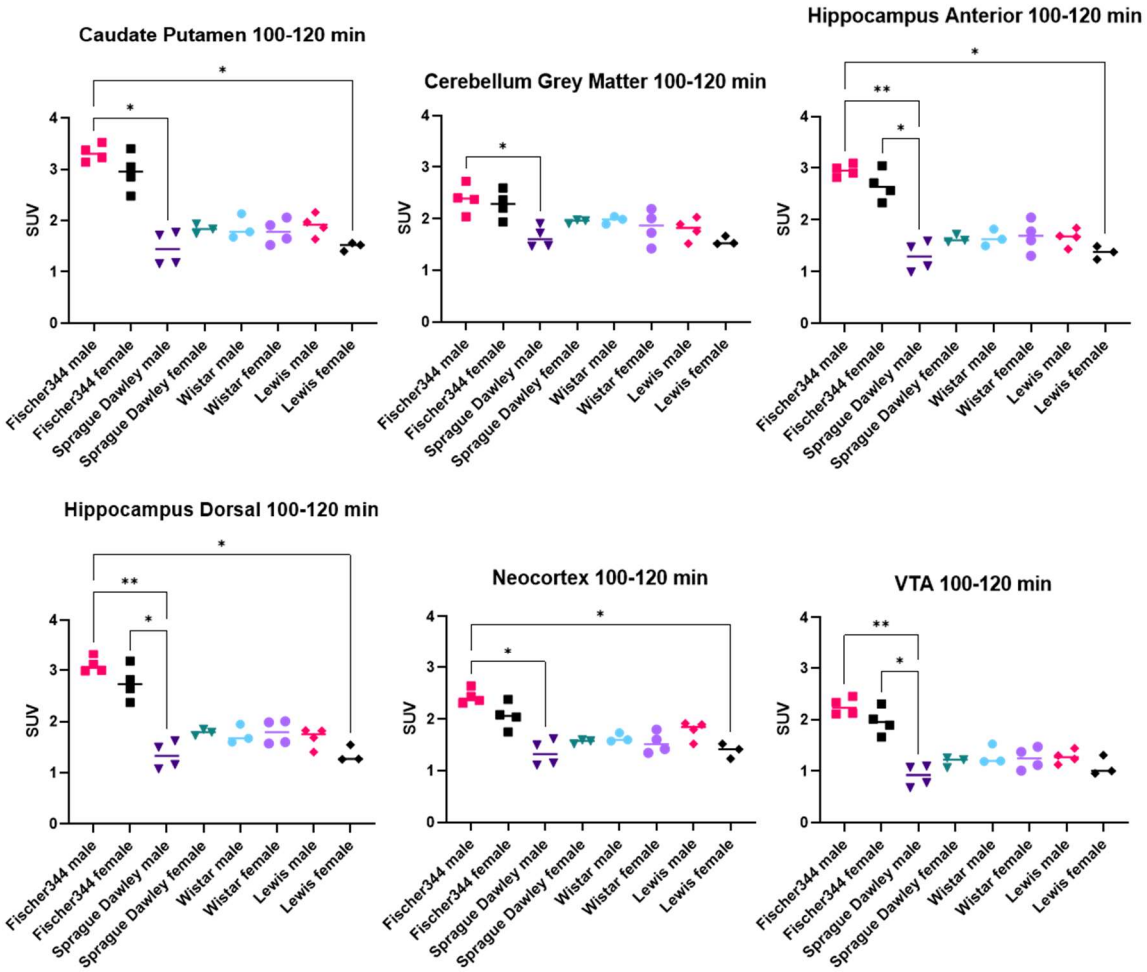

Figure 9. Standardize uptake values (SUVs) of the caudate putamen, cerebellum grey matter, hippocampus anterior and dorsal, neocortex and ventral tegmental area (VTA) at 100-120 min after [^{18}F]FPATPP injection. Data are presented with median line. Kruskal-Wallis test was conducted and significant (95% confidence interval) differences between strains are marked with *p ≤ 0.05, **p ≤ 0.01.

SUVs from different brain areas were compared to the pons, which was used as a reference region. This comparison is also connected to tracer's washout ratios. The highest ratios were detected in both sexes of Sprague Dawley compared to the other rat strains in the whole brain area (Figure 10.). In addition, Fischer344 had the lowest ratios in both sexes.

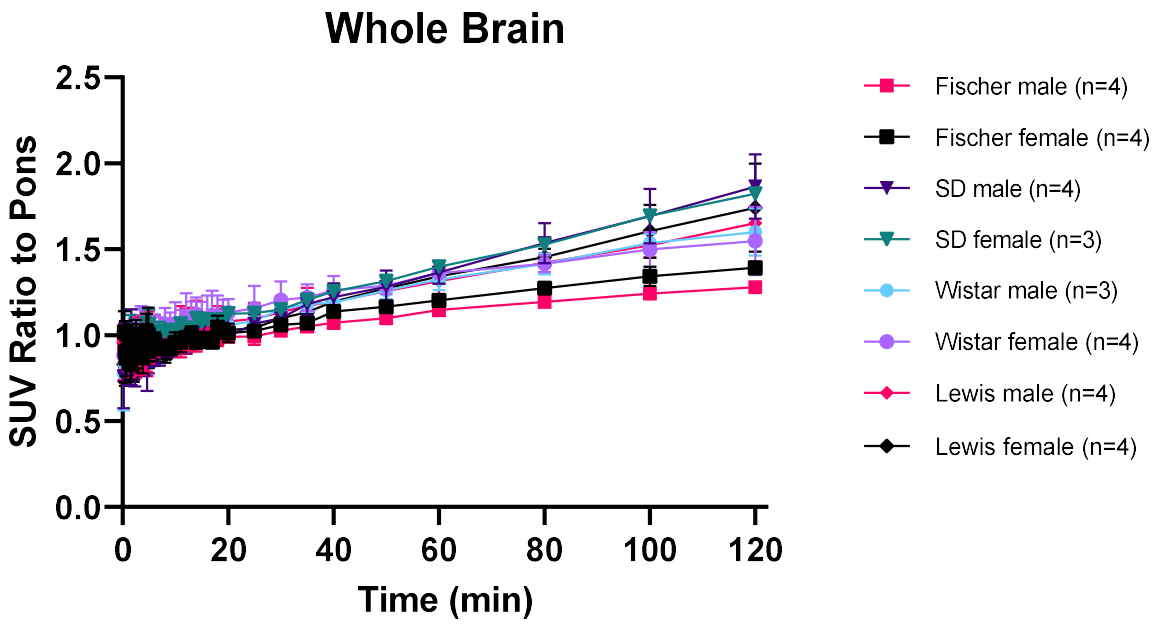

Figure 10. Standardize uptake value (SUV) ratios to pons in the whole brain area.

Ratios were examined more carefully in the last time frame, which was at 100-120 min after [^{18}F]FPATPP injection. The last time frame was picked to reach greater difference between groups. In the whole brain area, Fischer344 and Sprague Dawley male rats had a significant difference, which is seen in the Figure 11. The same difference was detected in the cerebellum grey matter and neocortex, and additionally difference between Fischer344 males and Sprague Dawley females was perceived in the cerebellum grey matter and dorsal part of the hippocampus (Figure 12).

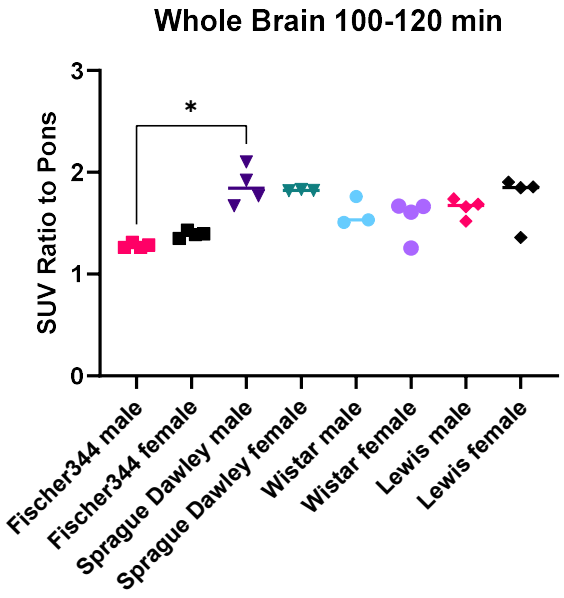

Figure 11. Standardize uptake value (SUV) ratio to pons of the whole brain area at 100-120 min after [^{18}F]FPATPP injection. Data are presented with median line. Kruskal-Wallis test was conducted and significant (95% confidence interval) differences between strains are marked with *p ≤ 0.05, **p ≤ 0.01.

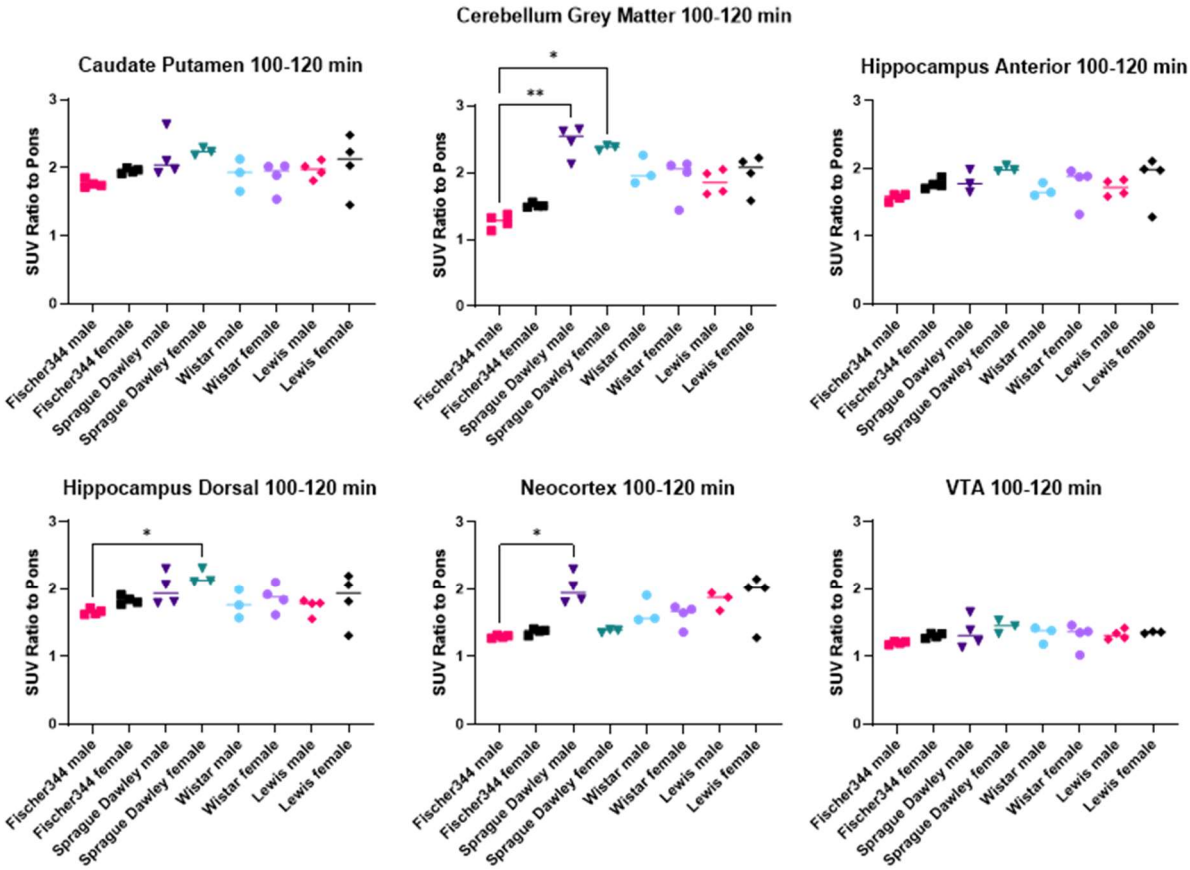

Figure 12. Standardize uptake value (SUV) ratios to pons of the caudate putamen, cerebellum grey matter, hippocampus anterior and dorsal, neocortex and ventral tegmental area (VTA) at 100-120 min after [^{18}F]FPATPP injection. Data are presented with median line. Kruskal-Wallis test was conducted and significant (95% confidence interval) differences between strains are marked with *p ≤ 0.05, **p ≤ 0.01.

2.2 *Ex vivo* autoradiography showed significant differences in tracer binding on the CB1R-rich regions

The results from *ex vivo* autoradiography were analyzed as the brain region of interest (ROI) ratios to pons. The different studied brain ROIs are shown in the Figure 13. For the analysis, the frontal cortex, caudate putamen, globus pallidus, entopeduncular nucleus, anterior and dorsal parts of the hippocampus, amygdala, anterior and dorsal parts of the substantia nigra, and cerebellum grey matter together with the reference region pons, were selected due to higher uptake in these regions.

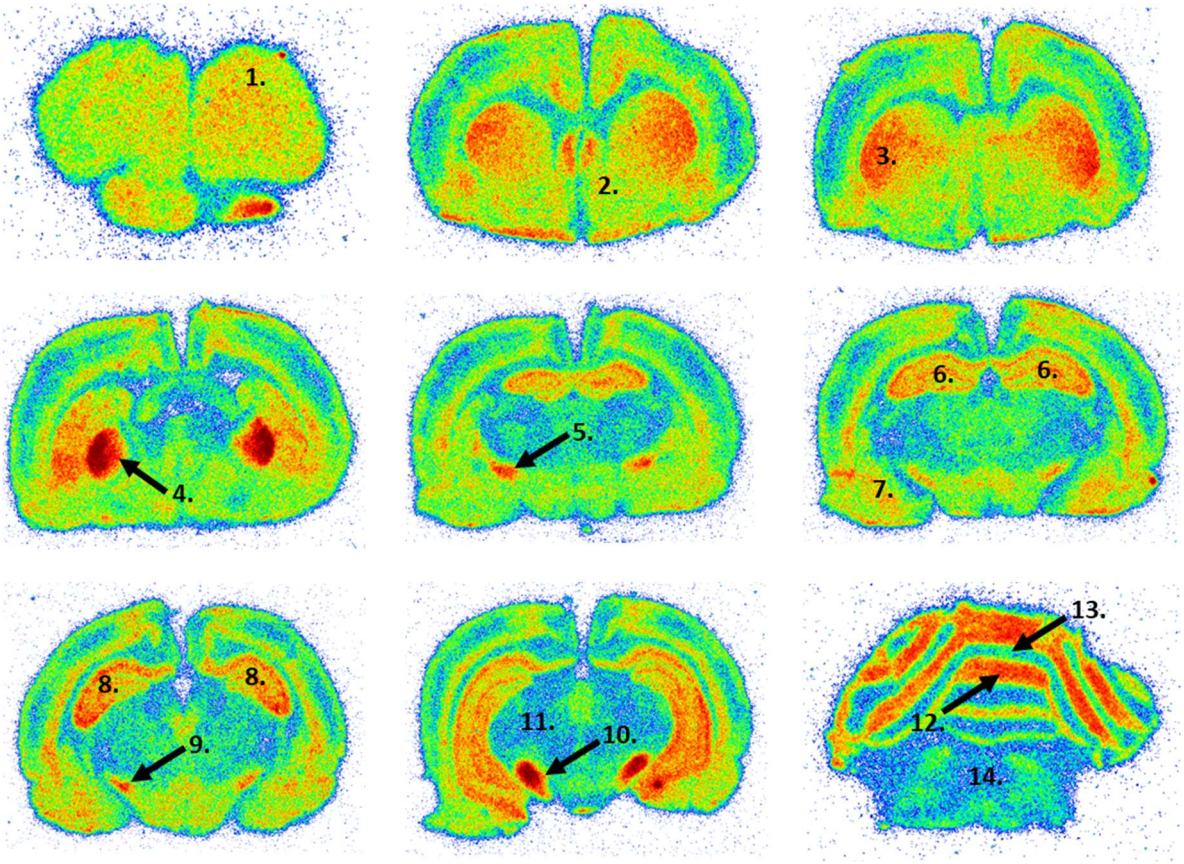

Figure 13. Selected brain regions for the analyses of ex vivo autoradiography data. 1. Frontal cortex, 2. nucleus accumbent, 3. caudate putamen, 4. globus pallidus, 5. entopeduncular nucleus, 6. hippocampus anterior, 7. amygdala, 8. hippocampus dorsal, 9. substantia nigra anterior, 10. substantia nigra dorsal, 11. thalamus, 12. cerebellum grey matter, 13. cerebellum white matter and 14. pons.

Differences in ratios were detected in every analyzed brain area (Figure 14). Fischer344 male rats had generally lower ratios than the other strains which is also seen as a significant difference in every brain area. Fischer344 male rats had a difference with Lewis female rats in most of the brain regions, and moreover with Sprague Dawley female and male rats. More significant differences (**$p \leq 0.01$) were detected in the globus pallidus, substantia nigra's dorsal part and cerebellum grey matter which are also visually ones of the highest uptake regions in the brain, as seen in the Figure 13.

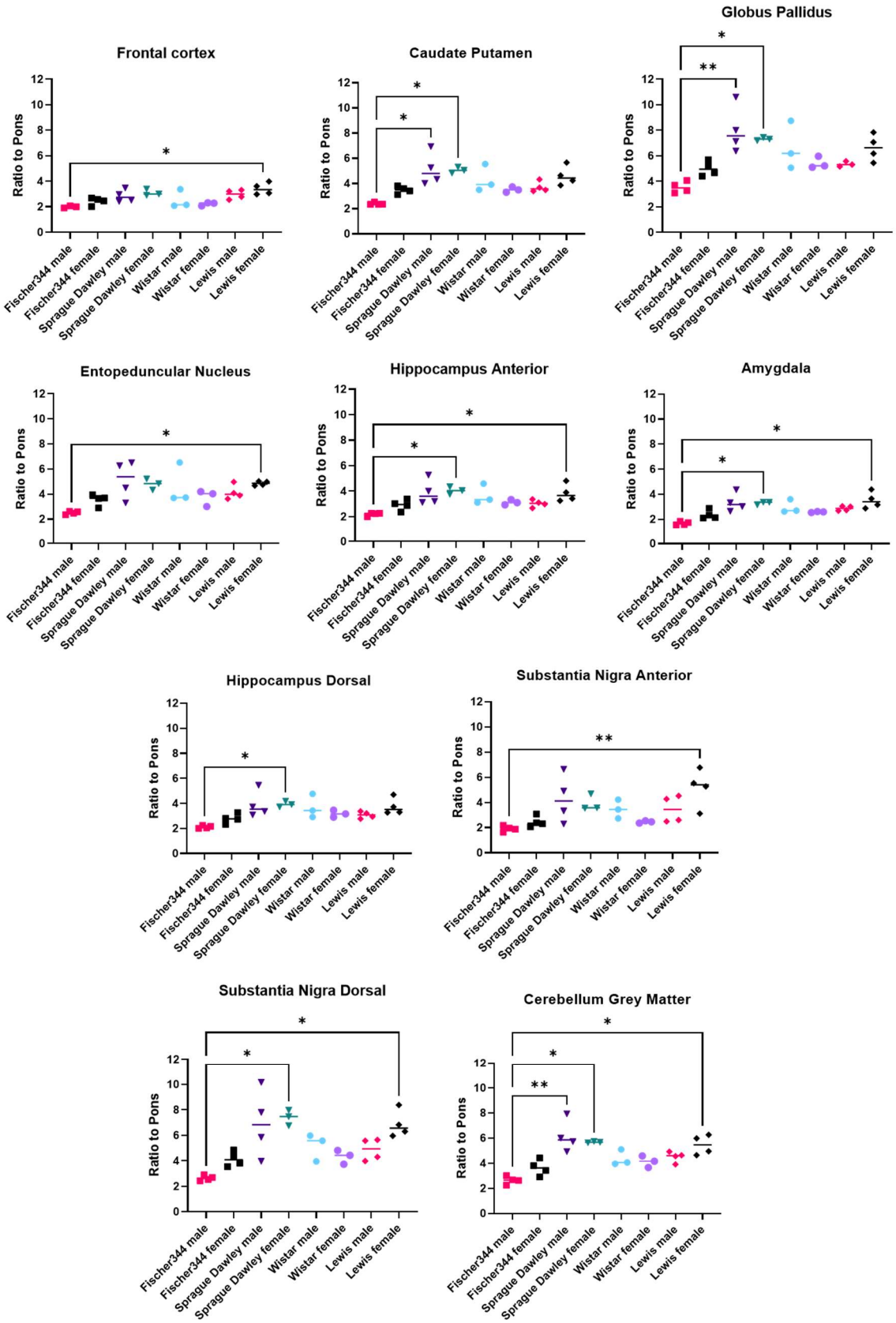

Figure 14. Ex vivo autoradiography ratios to pons of the frontal cortex, caudate putamen, globus pallidus, entopeduncular nucleus, hippocampus anterior and dorsal, amygdala, substantia nigra anterior and dorsal, and cerebellum grey matter. Data are presented with median line. Kruskal-Wallis test was conducted and significant (95% confidence interval) differences between strains are marked with *p ≤ 0.05, **p ≤ 0.01.

2.3 *Ex vivo* biodistribution uptake was detected in the CB1R-rich organs and in the metabolic organs

The [^{18}F]FPATPP uptake in the peripheral organs was measured 120 minutes after tracer injection. Eight rats of Fischer344 were used and sexes were pooled, since there was no sex difference detected. High tracer uptake (SUV more than 2) was measured in the bone marrow, lung, brain, cerebellum, cortex, brown adipose tissue, Harderian gland, adrenals, liver, stomach, and small intestine whereas low uptake was measured in blood, plasma, erythrocytes, bone, and eyes. Results are seen in the Figure 15.

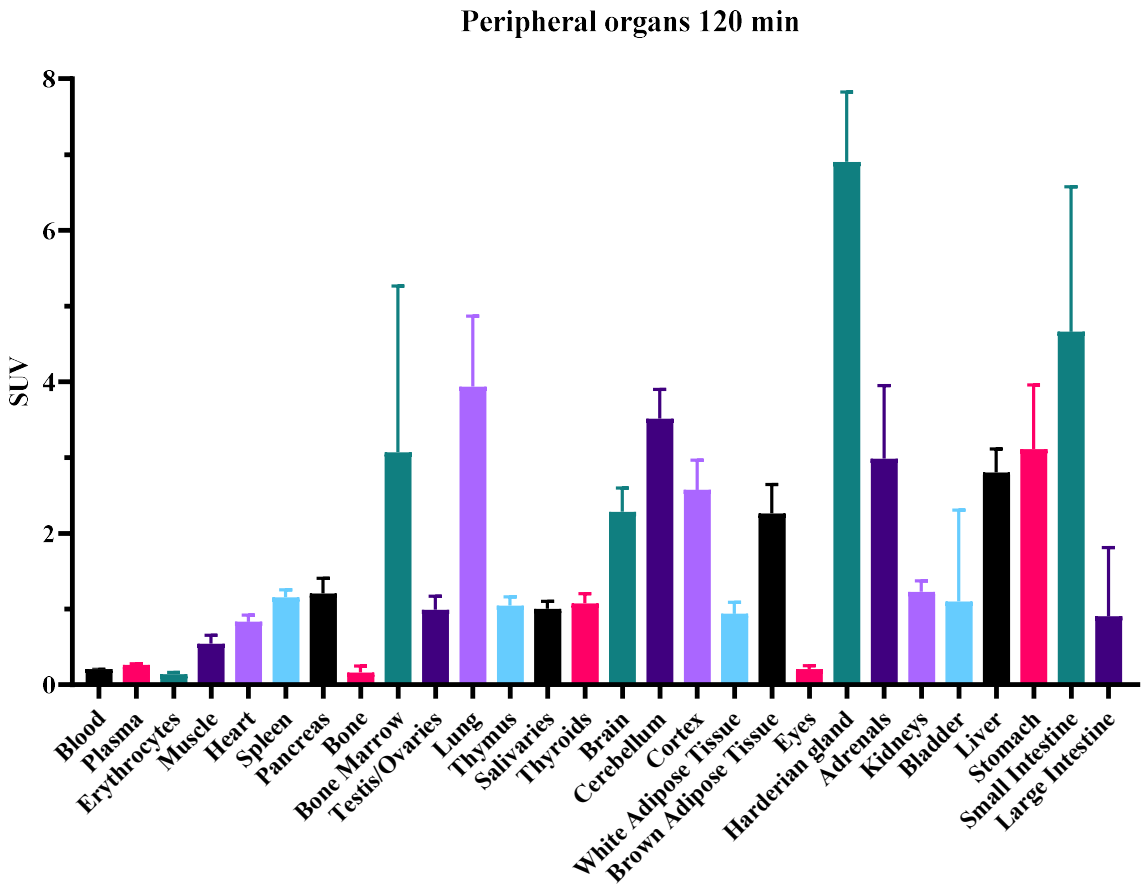

Figure 15. Standardized uptake values (SUV) measured from the tissues and organs 120 min after [18F]FPATPP injection. Values are presented as the mean ± SD. n = 8.

3 Discussion

The objective of this study was to investigate the pharmacokinetics of the CB1R-specific tracer [^{18}F]FPATPP in four different rat strains, Fischer344, Sprague Dawley, Wistar and Lewis, and both in sexes. *In vivo* PET/CT imaging and *ex vivo* brain autoradiography were used to measure tracer uptake in the brain and peripheral tissues and organs, which were collected for further analysis.

The PET imaging results, obtained *in vivo*, revealed significant differences between sexes and strains in all the analyses. Comparing Fischer344 and Sprague Dawley rats, the highest differences were observed. The AUC data for SUV time-activity, and peak/120 min ratios indicated that the initial tracer uptake and washout varied considerably between strains, particularly when Fischer344 rats were compared to the other rat strains. Moreover, SUV ratios in CB1R-rich areas exhibited higher uptake in Fischer344 rats compared to Sprague Dawley rats, while Lewis and Wistar rats had more balanced ratios. Overall, Fischer344 rats exhibited the highest initial tracer uptake, while Sprague Dawley male rats showed the fastest washout in the brain. This data provides valuable insights into the pharmacokinetics of [^{18}F]FPATPP in rats, and it also highlights the need to balance two important tracer features, uptake, and washout.

The primary findings of the *ex vivo* brain autoradiography data showed notable differences in the binding of [^{18}F]FPATPP among male Fischer 344 rats compared to the other strains. Notably, the differences in binding were observed in both males and females. The most significant variations in binding were detected in the areas that are known to be rich in CB1R, such as the globus pallidus, dorsal part of the substantia nigra, and the grey matter of the cerebellum. Unlike previous studies by Takkinen and Lahdenpohja that used the thalamus as a reference region for studying [^{18}F]FMPEP-d2 and [^{18}F]FPATPP in mice, this study used the pons as a pseudo-reference region (Takkinen et al., 2018; Lahdenpohja et al., 2020). While the thalamus was also analyzed, the pons was deemed cleaner due to lower noise levels from the other regions. This difference in reference region selection could be attributed to the larger size of the rat brain compared to that of the mouse.

In the results of biodistribution analysis, the highest uptake of [^{18}F]FPATPP was observed in the Harderian glands behind the eyes. This accumulation is not related to the CB1Rs and is a common phenomenon observed with most PET tracers (Kiessling et al., 2017). In terms of

the known CB1R-rich areas, high uptake was detected in the brown adipose tissue, adrenals, bone marrow and brain, which also correlates with both *in vivo* and *ex vivo* autoradiography data. However, high uptake in the liver, stomach, and small intestine suggests that the tracer and its metabolites are eliminated through fecal excretion. In other words, the tracer is excreted via the hepatobiliary route. Moreover, the low uptake in the bone indicates minimal defluorination, which is a positive finding for the tracer. Notably, there was a low uptake in the blood, indicating efficient distribution of [^{18}F]FPATPP to organs and tissues 120 minutes after injection.

As [^{18}F]FPATPP has not been previously studied in rats, the information gathered in this study regarding its pharmacokinetics will be valuable for future CNS drug studies utilizing rats as disease models. Rats are advantageous in this context due to their larger size compared to mice, making it easier to analyze small brain regions using PET imaging. Additionally, certain models of human diseases, such as some cardiovascular and nutritional diseases, are more faithful and relevant when studied in rats (Szpirer, 2022). Examining both inbred and outbred rat models will contribute to a more comprehensive understanding of the optimal animal model for specific disease models.

All rat strains used in this study are well-established and commonly used, providing a reliable platform for disease models. While Sprague Dawley and Wistar rats are outbred strains, Lewis and Fischer344 rats are inbred strains, highlighting a fundamental difference between these strains (Taconic Biosciences, 2021). The results of this study suggest differences between the strains, particularly with Fischer344 and Sprague Dawley rats. This could be attributed to their inbred and outbred natures. However, if this hypothesis is true, there should have also been a difference between Wistar and Lewis rats, indicating that further studies on pharmacokinetics are required to shed light on this matter.

This project did not encounter any major drawbacks, but there were some minor issues, such as the death of one animal and the need to allocate a small amount of tracer between ongoing studies. Fortunately, extra animals and imaging days were arranged to complete the planned group sizes. However, since this study had a basic research nature, a relatively small number of animals per group was used, and future studies will be required to confirm and draw conclusive results from the current findings.

Additionally, further studies are needed to understand the complete pharmacokinetics of this tracer, including differences in metabolism, peripheral biodistribution, and excretion.

Radiometabolite analysis could clarify these pharmacokinetic differences and reveal possible differences in blood-brain-barrier permeability. Moreover, it would be beneficial to conduct blocking studies with a selective CB1R antagonist, such as rimonabant (Fong and Heymsfield, 2009), also in rats, at least with two different strains, such as Fischer344 and Sprague Dawley, with distinct backgrounds.

In conclusion, this study highlights the importance of considering strain and sex differences in tracer uptake and provides insights into the pharmacokinetics of [^{18}F]FPATPP. Further studies, such as radiometabolite analysis and blocking studies with a selective CB1R antagonist are needed to fully understand the tracer's pharmacokinetics in rats.

4 Materials and methods

4.1 Animals

Four different strains of rats were used in this study: Fischer344, Sprague Dawley, Wistar, and Lewis. Fischer and Sprague Dawley rats were provided from the Central Animal Laboratory of the University of Turku while Wistar and Lewis rats were ordered from Janvier Labs (Le Genest-Saint-Isle, France). All the animals were two to three months old, and weight of the male rats was 269 ± 45 g and female rats 228 ± 9 g.

Rats were group housed at the Central Animal Laboratory of the University of Turku under standardized conditions (temperature 21 ± 1.2 °C, humidity 55 ± 5%, lights on from 6:00 a.m. to 6:00 p.m.), with free access to certified standard laboratory soy-free chow (RM3 soya-free, 801710, Special Diets Service) and tap water. Professionally trained laboratory personnel according to the ethical guidelines of the International Council of Laboratory Animal Science (ICLAS) monitored animals daily. Animal experiments were conducted according to the Animal Research: Reporting of *in vivo* Experiments (ARRIVE) guidelines (Percie du Sert et al., 2020) and the ethical permission for all studies has been obtained from the State Provincial Offices of Finland (ESAVI/16273-2019).

4.2 Study design

Every animal went through the same steps, which are illustrated in the Figure 16. Study design: A) Intravenous injection of [^{18}F]FPATPP tracer, B) Computerized tomography (CT) + 120 min dynamic PET scan, C) Cryo-sectioning, D) Scanning with imaging plate reader, E) PET image data for analysis, F) Autoradiography data for analysis. The number of animals used in this study is indicated in Table 5. The exclusion criteria were either a poor injection or unexpected death of the animal after tracer injection.

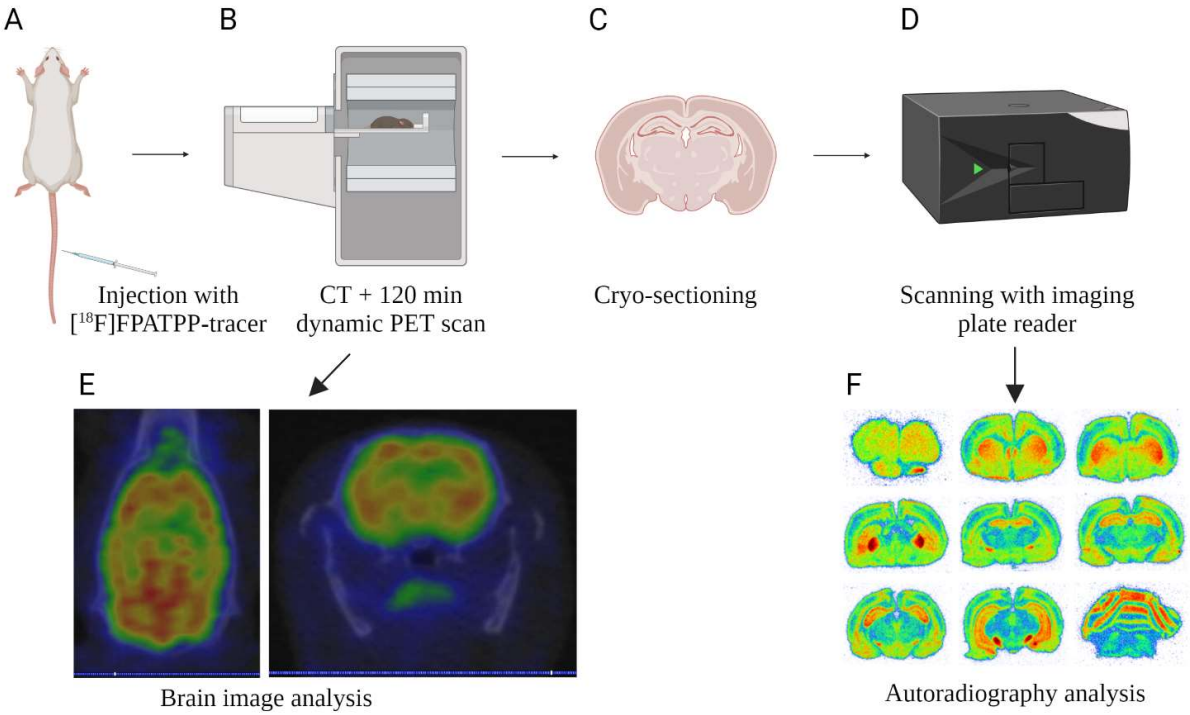

Figure 16. Study design: A) Intravenous injection of [^{18}F]FPATPP tracer, B) Computerized tomography (CT)+ 120 min dynamic positron emission tomography (PET) scan, C) Cryo-sectioning, D) Scanning with imaging plate reader, E) PET image data for analysis, F) Autoradiography data for analysis. Created with BioRender.com.

Table 5. Overview of the animal strain, total number, sex, and exclusion number and criteria of animals used in this work. Exclusion criteria were either (a) a poor injection or (b) unexpected death of the animal after tracer injection. n = number of animals.

Strain	n	Sex	Excluded
Fischer344	4	Female	-
Fischer344	4	Male	-
Sprague Dawley	4	Female	1 (a)
Sprague Dawley	4	Male	-
Wistar	4	Female	1 (a)
Wistar	4	Male	1 (b)
Lewis	4	Female	1 (a)
Lewis	4	Male	-

4.2.1 Tracer production

Nine batches of [^{18}F]FPATPP tracer were used for this study. [^{18}F]FPATPP was synthesized as previously published (Lahdenpohja et al., 2020). The radiochemical purity of the final product was over 99% for all the baches at the end of synthesis and molar activity was 145 ± 128 GBq/μmol (n = 31).

4.2.2 *In vivo* PET imaging

The *in vivo* PET imaging was performed for each rat using [^{18}F]FPATPP as a PET tracer. Dynamic scans of 120 min were performed to study the distribution and accumulation of [^{18}F]FPATPP in the brain in the different strains including the SUV time activity curves and target-to-reference tissue ratios.

All the study animals were handled the same way to avoid stress before study actions. The imaging was performed using an Inveon multimodality PET/CT (Siemens Medical Solutions) small animal scanner. The rats were anaesthetized with an isoflurane/oxygen mixture (induction 4% and maintenance 2.5%) on a heating pad approximately 30 min prior to tracer injection. The rats were injected between 10 am to 3 pm before which they had free access to food and water. CT imaging was performed for attenuation correction of the PET data, and to obtain an anatomical reference for the PET images. Then, [^{18}F]FPATPP (20 ± 5 MBq, injected mass 2033 ± 3417 ng/kg) was injected via tail vein, and 120 min dynamic three-dimensional PET list mode scans with an energy window of 350-650 keV was performed. The PET list mode data were reconstructed using the frame sequence 30 x 10 s, 15 x 60 s, 4 x 300 s, 2 x 600 s and 3 x 1200 s, and ordered subset expectation maximization (OSEM-3D) algorithm.

The *in vivo* PET images were analyzed using in-house developed analysis software implemented in MATLAB. The SUVs (SUV_{BW}=C_{PET}[T]/[Dose/Weight]) of seven brain ROIs (the caudate putamen, hippocampus anterior and dorsal, ventral tegmental area [VTA], cerebellum grey matter, neocortex and whole brain) were further processed into figures as well as ratios of SUVs of those ROIs to reference tissue pons.

4.2.3 *Ex vivo* autoradiography

After the *in vivo* PET imaging, the rats were sacrificed in deep isoflurane (4% isoflurane/oxygen gas) anesthesia by heart puncture and perfused with physiological saline (0.9% NaCl-solution; B. Braun, Melsungen, Germany). Immediately after this, the brains were removed, weighed,

frozen in dry ice chilled isopentane (2-methylbutane; Sigma-Aldrich), and cut into 20-µm thick coronal cryosections in nine different brain regions with a CM3050S cryostat (Leica Biosystems, Germany). Cryosections on the microscope slides were air-dried and exposed to imaging plates (Fuji BAS Imaging Plate TR2025, Fuji Photo Film Co., Ltd., Tokyo, Japan) for minimum two half-lives of fluorine-18.

The radioactivity distribution on the imaging plates were digitized with BAS5000 analyser (Fujifilm Lifesciences, Japan). The digitalized images were analyzed using Aida Image Analysis software (Image Analyzer v. 4.22: Raytest Isotopenmessgeräte GmbH, Straubenhardt, Germany). The main ROIs, 13 as total, were chosen for quantification. The sections were analyzed as photostimulated luminescence/area – background (PSL/mm^2) for brain ROIs (the frontal cortex, caudate putamen, globus pallidus, entopeduncular nucleus, hippocampus anterior and dorsal, substantia nigra anterior and dorsal, and cerebellum grey matter) and reference region (the pons).

4.2.4 *Ex vivo* biodistribution

Fischer344 (n = 8) rats were anaesthetized with isoflurane/oxygen mixture (induction 4% and maintenance 2.5%) on a heating pad approximately 30 min prior to tracer injection. [^{18}F]FPATPP was injected intravenously into a tail vein and after 120 min, the rats were sacrificed in deep isoflurane (4% isoflurane/oxygen gas) anesthesia by heart puncture and perfused with physiological saline (0.9% NaCl-solution; B. Braun, Melsungen, Germany). A variety of organs and tissues (blood, bone [parietal], brain, adrenals, plasma, bone marrow [from tibia], cerebellum, kidneys, erythrocytes, testis/ovaries, cortex, bladder [incl. urine], muscle [from hind leg], lung, white adipose tissue, liver, heart, thymus, brown adipose tissue, stomach with contents, spleen, salivaries [submandibular glands], eyes, small intestine with contents, pancreas, thyroids, Harderian glands and large intestine with contents) were removed from the body, weighted, and measured for radioactivity using a 2480 Wizard2 automatic gamma counter (PerkinElmer, Turku, Finland).

4.2.5 Statistics

The results were expressed as mean ± standard deviation (SD). Kruskal-Wallis test was used for the statistical analysis of both SUV data and autoradiography data. AUC results were calculated with one-way analysis of variance (ANOVA) and Tukey´s multiple comparison test. The statistical analyses were performed in GraphPad Prism 9.3.1. and all tests were performed with the significance level set at 0.05.

5 Acknowledgements

I would like to thank Francisco López-Picón and Merja Haaparanta-Solin for supervision during this project and patience with my writing process. Thanks go also to Aake Honkaniemi, Mira Eisala, Marko Vehmanen and other members of Turku PET Centre Preclinical Imaging Unit for their technical support in the laboratory. I would like to acknowledge people from radiochemistry for the tracer synthesis and delivery for multiple times. In addition, thanks to people of Central Animal Laboratory of the University of Turku for animal care and maintenance during this project.

I would also like to thank Heidi Nykänen, Isabel Kern and Jessika Ständer who were my fellow thesis workers at Turku PET Centre at the time of this project. In addition, special thanks to my family and friends for supporting me with this thesis.

6 List of Abbreviations

[^{11}C]-MePPEP	(3*R*,5*R*)-5-(3-[^{11}C]methoxyphenyl)-3-[(*R*)-1-phenylethylamino]-1-(4-trifluoromethylphenyl)
[^{18}F]MK-9470	*N*-{(1*S*,2S)-2-(3-cyanophenyl)-3-[4-(2-[^{18}F]fluoroethoxy)-phenyl]-1-methylpropyl}-2-methyl-2-[(5-methylpyridin-2-yl)-oxy]propanamide
[^{18}F]FMPEP-*d2*	(3*R*,5*R*)-5-(3-([^{18}F]fluoromethoxy)-phenyl)-3-(((*R*)-1-phenylethyl)amino)-1-(4-(trifluoromethyl)-phenyl)pyrrolidin-2-one
[^{18}F]FPATPP	(3*R*,5*R*)-5-(3-[^{18}F]fluorophenyl)- 3-(((*R*)-1-phenylethyl)amino)-1-(4-(trifluoromethyl)phenyl)- pyrrolidin-2-one
2-AG	2-arachidonoyl-glycerol
AEA	Anandamide
ANOVA	Analysis of Variance
ARRIVE	Animal Research: Reporting of *in vivo* Experiments
CB1R	Cannabinoid 1 Receptor
CB2R	Cannabinoid 2 Receptor
CNS	Central Nervous System
CT	Computerized tomography
ICLAS	International Council of Laboratory Animal Science
OSEM-3D	Ordered Subset Expectation Maximization
PET	Positron Emission Tomography
PSL	Photo Stimulated Intensity
ROI	Regions of Interest
SUV	Standardized Uptake Value
SD	Standard Deviation
SE	Standard Error

THC	Δ9-tetrahydrocannabinol
VTA	Ventral Tegmental Area

7 References

Beyzavi, M.H., D. Mandal, M.G. Strebl, C.N. Neumann, E.M. D'Amato, J. Chen, J.M. Hooker, and T. Ritter. 2017. 18F-Deoxyfluorination of Phenols via Ru π-Complexes. *ACS Cent Sci*. 3. doi:10.1021/acscentsci.7b00195.

Brammer, D.W., J.M. Riley, S.C. Kreuser, K.R. Zasadny, M.J. Callahan, and M.D. Davis. 2007. Harderian gland adenectomy: A method to eliminate confounding radio-opacity in the assessment of rat brain metabolism by 18F-fluoro-2-deoxy-D-glucose positron emission tomography. *Journal of the American Association for Laboratory Animal Science*. 46.

Burns, H.D., K. van Laere, S. Sanabria-Bohórquez, T.G. Hamill, G. Bormans, W.S. Eng, R. Gibson, C. Ryan, B. Connolly, S. Patel, S. Krause, A. Vanko, A. van Hecken, P. Dupont, I. de Lepeleire, P. Rothenberg, S.A. Stoch, J. Cote, W.K. Hagmann, J.P. Jewell, L.S. Lin, P. Liu, M.T. Goulet, K. Gottesdiener, J.A. Wagner, J. de Hoon, L. Mortelmans, T.M. Fong, and R.J. Hargreaves. 2007. [18F]MK-9470, a positron emission tomography (PET) tracer for in vivo human PET brain imaging of the cannabinoid-1 receptor. *Proc Natl Acad Sci U S A*. 104. doi:10.1073/pnas.0703472104.

Cohen, R.M., K. Rezai-Zadeh, T.M. Weitz, A. Rentsendorj, D. Gate, I. Spivak, Y. Bholat, V. Vasilevko, C.G. Glabe, J.J. Breunig, P. Rakic, H. Davtyan, M.G. Agadjanyan, V. Kepe, J.R. Barrio, S. Bannykh, C.A. Szekely, R.N. Pechnick, and T. Town. 2013. A transgenic alzheimer rat with plaques, tau pathology, behavioral impairment, oligomeric Aβ, and frank neuronal loss. *Journal of Neuroscience*. 33. doi:10.1523/JNEUROSCI.3672-12.2013.

Devane, W.A., F.A. Dysarz, M.R. Johnson, L.S. Melvin, and A.C. Howlett. 1988. Determination and characterization of a cannabinoid receptor in rat brain. *Mol Pharmacol*. 34.

Donohue, S.R., J.H. Krushinski, V.W. Pike, E. Chernet, L. Phebus, A.K. Chesterfield, C.C. Felder, C. Halldin, and J.M. Schaus. 2008. Synthesis, ex vivo evaluation, and radiolabeling of potent 1,5-diphenylpyrrolidin-2-one cannabinoid subtype-1 receptor ligands as candidates for in vivo imaging. *J Med Chem*. 51. doi:10.1021/jm800416m.

Eriksson, O., K. Mikkola, D. Espes, L. Tuominen, K. Virtanen, S. Forsbäck, M. Haaparanta-Solin, J. Hietala, O. Solin, and P. Nuutila. 2015. The cannabinoid

receptor-1 is an imaging biomarker of brown adipose tissue. *Journal of Nuclear Medicine*. 56. doi:10.2967/jnumed.115.156422.

Fong, T.M., and S.B. Heymsfield. 2009. Cannabinoid-1 receptor inverse agonists: Current understanding of mechanism of action and unanswered questions. *Int J Obes*. 33. doi:10.1038/ijo.2009.132.

Gruden, G., F. Barutta, G. Kunos, and P. Pacher. 2016. Role of the endocannabinoid system in diabetes and diabetic complications. *Br J Pharmacol*. 173. doi:10.1111/bph.13226.

Hargreaves, R.J., and E.A. Rabiner. 2014. Translational PET imaging research. *Neurobiol Dis*. 61. doi:10.1016/j.nbd.2013.08.017.

Hirvonen, J., P. Zanotti-Fregonara, J.C. Umhau, D.T. George, D. Rallis-Frutos, C.H. Lyoo, C.T. Li, C.S. Hines, H. Sun, G.E. Terry, C. Morse, S.S. Zoghbi, V.W. Pike, R.B. Innis, and M. Heilig. 2013. Reduced cannabinoid CB 1 receptor binding in alcohol dependence measured with positron emission tomography. *Mol Psychiatry*. 18. doi:10.1038/mp.2012.100.

Hooker, J.M., and R.E. Carson. 2019. Human Positron Emission Tomography Neuroimaging. *Annu Rev Biomed Eng*. 21. doi:10.1146/annurev-bioeng-062117-121056.

Howlett, A.C., F. Barth, T.I. Bonner, G. Cabral, P. Casellas, W.A. Devane, C.C. Felder, M. Herkenham, K. Mackie, B.R. Martin, R. Mechoulam, and R.G. Pertwee. 2002. International Union of Pharmacology. XXVII. Classification of cannabinoid receptors. *Pharmacol Rev*. 54. doi:10.1124/pr.54.2.161.

di Iorio, G., M. Lupi, F. Sarchione, I. Matarazzo, R. Santacroce, F. Petruccelli, G. Martinotti, and M. di Giannantonio. 2013. The Endocannabinoid System: A Putative Role in Neurodegenerative Diseases. *Int J High Risk Behav Addict*. 2. doi:10.5812/ijhrba.9222.

Kiessling, F., B.J. Pichler, and P. Hauff. 2017. Small animal imaging : basics and practical guide. Second edition. F. Kiessling, B.J. Pichler, and P. Hauff, editors. Springer, Cham, Switzerland.

Lahdenpohja, S., N.A. Rajala, J.S. Helin, M. Haaparanta-Solin, O. Solin, F.R. López-Picón, and A.K. Kirjavainen. 2020. Ruthenium-Mediated 18F-Fluorination and Preclinical Evaluation of a New CB1Receptor Imaging Agent [18F]FPATPP. *ACS Chem Neurosci*. 11. doi:10.1021/acschemneuro.0c00313.

Lowe, H., N. Toyang, B. Steele, J. Bryant, and W. Ngwa. 2021. The endocannabinoid system: A potential target for the treatment of various diseases. *Int J Mol Sci*. 22. doi:10.3390/ijms22179472.

Mechoulam, R., and L.A. Parker. 2013. The endocannabinoid system and the brain. *Annu Rev Psychol*. 64. doi:10.1146/annurev-psych-113011-143739.

Moldrich, G., and T. Wenger. 2000. Localization of the CB1 cannabinoid receptor in the rat brain. An immunohistochemical study. *Peptides (N.Y.)*. 21. doi:10.1016/S0196-9781(00)00324-7.

Ohno-Shosaku, T., T. Maejima, and M. Kano. 2001. Endogenous cannabinoids mediate retrograde signals from depolarized postsynaptic neurons to presynaptic terminals. *Neuron*. 29. doi:10.1016/S0896-6273(01)00247-1.

Pagotto, U., G. Marsicano, D. Cota, B. Lutz, and R. Pasquali. 2006. The emerging role of the endocannabinoid system in endocrine regulation and energy balance. *Endocr Rev*. 27. doi:10.1210/er.2005-0009.

Percie du Sert, N., V. Hurst, A. Ahluwalia, S. Alam, M.T. Avey, M. Baker, W.J. Browne, A. Clark, I.C. Cuthill, U. Dirnagl, M. Emerson, P. Garner, S.T. Holgate, D.W. Howells, N.A. Karp, S.E. Lazic, K. Lidster, C.J. MacCallum, M. Macleod, E.J. Pearl, O.H. Petersen, F. Rawle, P. Reynolds, K. Rooney, E.S. Sena, S.D. Silberberg, T. Steckler, and H. Würbel. 2020. The ARRIVE guidelines 2.0: Updated guidelines for reporting animal research*. *Journal of Cerebral Blood Flow and Metabolism*. 40. doi:10.1177/0271678X20943823.

Pertwee, R.G. 2015. Endocannabinoids and their pharmacological actions. *In* Handbook of Experimental Pharmacology.

Qiao, J., C.M. Lawson, K.F.G. Rentrup, P. Kulkarni, and C.F. Ferris. 2020. Evaluating blood-brain barrier permeability in a rat model of type 2 diabetes. *J Transl Med*. 18. doi:10.1186/s12967-020-02428-3.

Rich, D.A. 1997. A brief history of positron emission tomography. *J Nucl Med Technol*. 25.

Surkin, P.N., S.L. Gallino, V. Luce, F. Correa, J.F. Solari, and A. De Laurentiis. 2018. Pharmacological augmentation of endocannabinoid signaling reduces the neuroendocrine response to stress. *Psychoneuroendocrinology*. 87. doi:10.1016/j.psyneuen.2017.10.015.

Syvänen, S., Ö. Lindhe, M. Palner, B.R. Kornum, O. Rahman, B. Långström, G.M. Knudsen, and M. Hammarlund-Udenaes. 2009. Species differences in blood-brain

barrier transport of three positron emission tomography radioligands with emphasis on P-glycoprotein transport. *Drug Metabolism and Disposition*. 37. doi:10.1124/dmd.108.024745.

Szpirer, C. 2022. Rat Models of Human Diseases and Related Phenotypes: A Novel Inventory of Causative Genes. *Mammalian Genome*. 33. doi:10.1007/s00335-021-09876-2.

Taconic Biosciences. 2021. NON-GEM MOUSE AND RAT STOCKS AND STRAINS. <https://www.taconic.com/find-your-model/non-gems/>. Data taken 14.9.2021.

Takkinen, J.S., F.R. López-Picón, A.K. Kirjavainen, R. Pihlaja, A. Snellman, T. Ishizu, E. Löyttyniemi, O. Solin, J.O. Rinne, and M. Haaparanta-Solin. 2018. [18 F]FMPEP-d 2 PET imaging shows age- and genotype-dependent impairments in the availability of cannabinoid receptor 1 in a mouse model of Alzheimer's disease. *Neurobiol Aging*. 69. doi:10.1016/j.neurobiolaging.2018.05.013.

Yasuno, F., A.K. Brown, S.S. Zoghbi, J.H. Krushinski, E. Chernet, J. Tauscher, J.M. Schaus, L.A. Phebus, A.K. Chesterfield, C.C. Felder, R.L. Gladding, J. Hong, C. Halldin, V.W. Pike, and R.B. Innis. 2008. The PET radioligand [11C]MePPEP binds reversibly and with high specific signal to cannabinoid CB1 receptors in nonhuman primate brain. *Neuropsychopharmacology*. 33. doi:10.1038/sj.npp.1301402.